Studies of electron diffusion in photo-excited Ni using time-resolved X-ray diffraction

A. Persson, Amélie Jarnac, Xiaocui Wang, H. Enquist, A. Jurgilaitis, J. Larsson

AIP | Applied Physics Letters

Studies of electron diffusion in photo-excited Ni using time-resolved X-ray diffraction

A. I. H. Persson, A. Jarnac, Xiaocui Wang, H. Enquist, A. Jurgilaitis, and J. Larsson

Citation: Applied Physics Letters **109**, 203115 (2016); doi: 10.1063/1.4967470
View online: http://dx.doi.org/10.1063/1.4967470
View Table of Contents: http://scitation.aip.org/content/aip/journal/apl/109/20?ver=pdfcov
Published by the AIP Publishing

Studies of electron diffusion in photo-excited Ni using time-resolved X-ray diffraction

A. I. H. Persson,[1] A. Jarnac,[1] Xiaocui Wang,[1] H. Enquist,[2] A. Jurgilaitis,[2] and J. Larsson[1,2,a)]
[1]*Department of Physics, Lund University, P.O. Box 118, SE-221 00 Lund, Sweden*
[2]*MAX IV Laboratory, Lund University, P.O. Box 118, SE-221 00 Lund, Sweden*

(Received 11 August 2016; accepted 22 October 2016; published online 18 November 2016)

We show that the heat deposition profile in a laser-excited metal can be determined by time-resolved X-ray diffraction. In this study, we investigated the electron diffusion in a 150 nm thick nickel film deposited on an indium antimonide substrate. A strain wave that mimics the heat deposition profile is generated in the metal and propagates into the InSb, where it influences the temporal profile of X-rays diffracted from InSb. We found that the strain pulse significantly deviated from a simple exponential profile, and that the two-temperature model was needed to reproduce the measured heat deposition profile. Experimental results were compared to simulations based on the two-temperature model carried out using commercial finite-element software packages and online dynamical diffraction tools. To reproduce the experimental data, the electron–phonon coupling factor was lowered compared to previously measured values. The experiment was carried out at a third-generation synchrotron radiation source using a high-brightness beam and an ultrafast X-ray streak camera with a temporal resolution of 3 ps. [http://dx.doi.org/10.1063/1.4967470]

When a material is photo-excited by an ultrashort laser pulse, the energy is initially deposited in the electron system and the photo-absorption varies exponentially with depth at low incident intensity. Before the electron and lattice systems reach thermal equilibrium, the electrons can diffuse, giving rise to a more complex energy–depth distribution. Electron diffusion in metals has been extensively studied using optical reflectivity measurements.[1–6] It has been observed that excited electrons in metals with low electron–phonon coupling factors, such as Au,[3] can move ballistically. In nickel on the other hand, the electron–phonon coupling factor is higher and the transport of heat into the sample is driven by the electron temperature gradient.[6,7] Time-resolved X-ray diffraction has been used previously to study strain/acoustic phonon generation in semiconductors and metals.[5,8–13] The advantage of using time-resolved X-ray diffraction, rather than optical reflectivity measurements, is that the strain profile can be probed, not only at the surfaces, but also inside the material.

In this study, we investigated the heat deposition profile in a thin nickel (Ni) film deposited on a bulk indium antimonide (InSb) (111-oriented) crystal. The heat deposition profile generates a strain pulse in Ni that is subsequently probed in the InSb crystal, see Fig. 1. By detecting the strain, it is possible to study the influence of the electronic transport on the heat deposition profile, which depends on parameters such as the electron–phonon coupling factor.[14] We have measured an acoustic response, similar to studies in which the change in optical reflectivity is measured. However, time-resolved optical reflectivity measurements are best suited for low-intensity excitation with an electron temperature increase below 100 K,[15] whereas the method described here is better suited for high-intensity excitation, with electron temperature exceeding 1000 K.

When a short laser pulse impinges on the surface of a material, the resulting heating and thermal expansion generate an acoustic strain pulse.[9,16] The energy of the laser pulse is deposited in the sample by the excitation of carriers (electrons), which equilibrate with the lattice within a few ps. The shape and amplitude of the heat deposition profile are determined by the optical absorption depth and the transport of photo-excited carriers before they thermalize with the lattice. Heating creates a static strain, and two strain waves that propagate in opposite directions.[16] The shape of the static strain and the two counter-propagating strain pulses are a replica of the heat deposition profile. The two propagating strain pulses have the opposite sign to the static strain profile, and half the amplitude, so the initial condition is that there is no strain. The pulse propagating towards the vacuum surface is reflected with an associated change of sign. On the short timescale during which this process was observed, only longitudinal expansion takes place. The strain entering in InSb

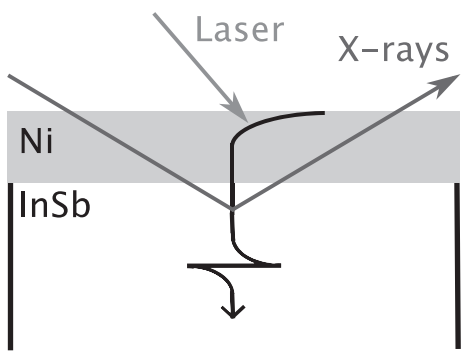

FIG. 1. The strain pulse generated in Ni propagates into InSb, where it is probed by time-resolved X-ray diffraction.

a)Author to whom correspondence should be addressed. Electronic mail: Jorgen.Larsson@fysik.lth.se

was investigated with time-resolved X-ray diffraction. The photon energy was tuned from the Bragg condition towards lower energies. Under these conditions, the initial compression wave is observed as a reduction in diffracted intensity. The shape of the initial response in the time-resolved X-ray diffraction curve depends on the shape of the strain pulse, and is sensitive to where the electrons deposit their energy in the lattice.

The experiments were carried out at beamline D611 at the now decommissioned 100 MHz storage ring MAX-II at the MAX IV Laboratory in Lund, Sweden. We pumped a thin Ni film deposited on an InSb (111) wafer using 50 fs laser pulses with a center wavelength of 800 nm. The thickness of the Ni film was 150 nm, which is significantly larger than the strain depths to be investigated. We probed InSb using X-rays with a set of energies near 4.51 keV. The Bragg condition for 4.51 keV is fulfilled at an incidence angle of 22°. The incidence angle of the laser was 37° with respect to the surface. The laser pulses were synchronized to a single electron bunch in the storage ring at a frequency of 4.25 kHz. The pulse duration of the X-ray bunch at the beamline was ~600 ps, and a streak camera was used to obtain the required time resolution of 3 ps. The X-ray beam and the laser beam were spatially overlapped on the sample. The laser fluence was 4 mJ/cm^2 incident on the sample with an uncertainty of about 30%, partly related to a non-Gaussian beam shape and experimental difficulties in maintaining laser/X-ray overlap during the measurement. The experimental setup has been described by Persson *et al.*[13] and the beamline is described in more detail by Harbst *et al.*[17]

A measured time-integrated energy scan is shown in Fig. 2. The energy scan has been normalized to the incoming X-ray intensity so the ordinate can be directly interpreted as X-ray diffraction efficiency. The time-resolved measurements were achieved by determining the diffracted intensity as a function of time for a given X-ray energy using the streak camera. The energy offset from the Bragg peak in the time-resolved X-ray measurements was −18 eV (indicated by the arrow in Fig. 2). Time-resolved data were acquired with and without laser excitation in order to facilitate normalization. The background-subtracted, normalized time-resolved X-ray diffraction efficiency is plotted in Fig. 3(a). Data was acquired

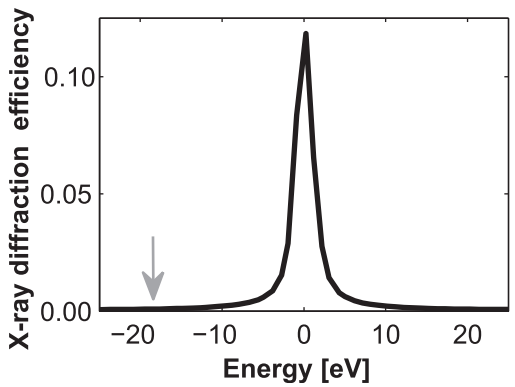

FIG. 2. Time-integrated energy scan obtained from InSb coated with a 150 nm Ni film. The scan was centered at an X-ray photon energy of 4.51 keV. The arrow indicates the −18 eV offset at which the time-resolved measurements were performed.

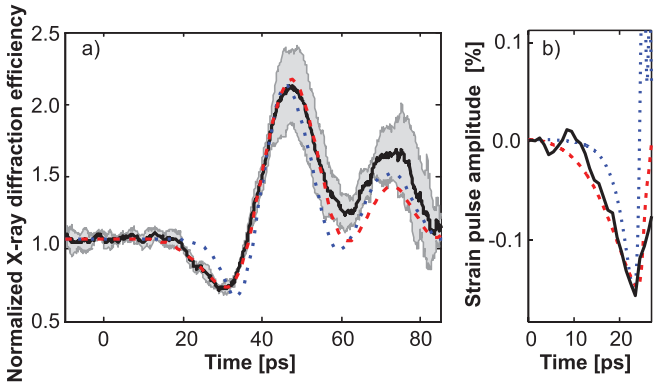

FIG. 3. (a) The experimental normalized X-ray diffraction efficiency (solid black line) was obtained as the ratio of acquisitions with and without laser excitation. The experimental data is shown together with calculated normalized X-ray diffraction efficiencies obtained from simulations using the two-temperature model and a value of $G = 9 \times 10^{16}$ W/m^3 K (red dashed line), and from a simple model including only heat conduction and an absorption depth of 17.6 nm (dotted blue line). (b) Derivative of the X-ray diffraction efficiency data which, under these conditions, gives the shape of the strain pulse, together with the strain pulses used for the simulations. The red dashed line shows the strain obtained with the two-temperature model, and the blue dotted line shows the strain when only the optical absorption depth and heat conduction are included. The strains are scaled on the TTM simulated strain, since the simplified analysis using only the derivative of the experimental X-ray diffraction efficiency only provides the shape of the strain pulse but not the amplitude.

as four separate datasets in order to check reproducibility. The solid black line shows the average X-ray diffraction efficiency from the four datasets obtained from the experiment. The measurement error is defined as the standard deviation for each time point of the four datasets and is shown as the light gray shaded area in Fig. 3(a). Each dataset consisted of approximately 400 000 X-ray pulses at 4.25 kHz when the laser was on, and 400 000 pulses when the laser was off. The total accumulation time for the data shown was 3 h.

In Fig. 3(a) the time delay between the laser excitation at 0 ps and the first change in X-ray diffraction efficiency after 25 ps is due to the time taken for the strain pulse to propagate through the Ni film. The first decrease in X-ray diffraction efficiency arises from the increased compression due to the strain pulse. The oscillatory part is predominantly associated with the sharp edge between the expansive and compressive strain as this edge is composed of a large range of phonon frequencies. As the edge enters the InSb the temporal manifestation of a selected phonon is seen as oscillations in the X-ray diffraction efficiency, which can be seen until this edge has left the X-ray probing depth.[8] The temporal range of most interest when studying electron diffusion is 20–35 ps. It is possible to visualize the strain pulse directly from the experimental data since the temporal shape of the X-ray diffraction efficiency can be intuitively estimated as the integral of the strain pulse. This estimation is due to the fact that the step function of the Ni/InSb interface serves as an integrator probing the parts of the strain that has entered into the X-ray scattering InSb. It relies on the assumption that the X-ray intensity can be approximated to depend linearly with the strain. This approximation is true for strains which are sufficiently small. Strained layers correspond to a shift of the energy scan (Fig. 2) and for small shifts the X-ray intensity changes approximately linearly with strain.

It should also be noted that this visualization is valid for short times only. When the sharp steplike feature arrives into the InSb, the phase-change of the reflected X-ray radiation from the differently strained lattice planes becomes too large. In this case, the approximation that the X-ray intensity is proportional to the strain is invalidated. Another issue with longer time delays is that the strain pulse may propagate so deep that the X-rays cannot probe the strained layers due to attenuation. A more detailed modelling as described below is, thus, needed to handle large strains and the full time evolution. In Fig. 3(b), we show the strain pulse as visualized by taking the derivative of the X-ray diffraction efficiency in the 0–30 ps temporal window (solid black line).

In order to understand the temporal shape of X-ray diffraction efficiency and explain how the laser energy is deposited as heat in the Ni sample, simulations were carried out by modeling the heat deposition in two different ways. In the first model, we included the tabulated thermal conductivity but not electron diffusion, while in the second model, we incorporated the electron diffusion by using the two-temperature model (TTM).[14,18] In the TTM, the electrons and lattice are treated as two separate systems. The energy from the laser pulse is transferred to the electrons, and the energy transfer between the two systems is governed by the electron–phonon coupling factor, G. The model is based on the following equations:

$$C_e\frac{\partial T_e(t,z)}{\partial t}=\frac{\partial}{\partial z}\left(\kappa\frac{\partial T_e(t,z)}{\partial z}\right)-G \times [T_e(t,z)-T_l(t,z)]+\frac{I}{\zeta}e^{-z/\zeta}e^{-t^2/\tau_p^2}, \quad (1a)$$

$$C_l\frac{\partial T_l(t,z)}{\partial t}=G\times[T_e(t,z)-T_l(t,z)], \quad (1b)$$

where C_e is the heat capacity per unit volume of electrons, which scales linearly with the electron temperature T_e, $C_e = A_e \times T_e$, where A_e is the electron heat capacity constant. $C_l = \rho \times c_l$ is the heat capacity per unit volume of the lattice, where ρ is the density of the material, and c_l its specific heat capacity. κ is the thermal conductivity, which is temperature dependent according to $\kappa = \kappa_0 T_e/T_l$, where κ_0 is the thermal conductivity at 300 K. T_l is the lattice temperature, ζ is the optical absorption depth, I is the absorbed laser intensity and τ_p is the laser pulse duration.

After calculating the lattice temperature profile $T_l(t,z)$, it was imported into Comsol® and used to calculate the strain generation in Ni, subsequent propagation to the interface and finally the strain transmission at the interface and propagation in InSb with a temporal resolution of 0.1 ps.[13] The time dependent strain profile was sent to Sergey Stepanov's X-ray server,[19] where the time-resolved X-ray diffraction efficiency from InSb was calculated. The values used in the simulations are listed in Table I. Finally, the results were analyzed in MATLAB®, where they were first convoluted in energy with a Voigt profile with a full width at half maximum (FWHM) of 7 eV in order to account for the spectral content and divergence of the X-ray beam, and subsequently in time with a Gaussian having a FWHM of 3 ps corresponding to the temporal response function of the streak camera. This procedure gives the same results as the udkm1Dsim toolbox.[20]

TABLE I. The properties of nickel and InSb used in the simulations.

Parameter	Ni	InSb
Electron heat capacity constant, A_e [J/m^3 K^2]	1065[a]	…[e]
Thermal conductivity, κ_0 [W/m K]	90.7[b]	…[e]
Optical absorption depth, 800 nm, ζ [nm]	17.6[c]	…[e]
Lattice specific heat capacity, c_l [J/kg K]	444[b]	…[e]
Density, ρ [kg/m^3]	8900[b]	5774.7[b]
Speed of longitudinal acoustic mode [m/s]	6040[c]	3880[d]
$2d_{111}$ spacing [Å]	…[e]	7.47[f]

[a]Kittel.[26]
[b]*Handbook of Chemistry and Physics*.[27]
[c]Saito *et al*.[23]
[d]Slutsky and Garland.[28]
[e]Parameter not relevant in the model.
[f]Based on lattice constant $a = 6.47$ Å.[29]

The simulated time-resolved X-ray diffraction efficiency using two different models for the heat conduction are shown in Fig. 3(a). The dotted blue line is obtained from the model using only the thermal conductivity. The dashed red line is obtained from the TTM. In Fig. 3(b), we compare the strain pulses calculated with the thermal conductivity model (dotted blue line) and with the two-temperature model (dashed red line) to the experimental strain (solid black line). The strain pulses are normalized to the amplitude of the strain calculated with the TTM. The fact that the strain pulse used in the simulation is in good agreement with the derivative of the data shows that the shape of the strain pulse can be obtained directly from the time-resolved data.

As can be seen, a reasonable match to the data cannot be obtained without including the electron diffusion. As discussed below the simulations of the X-ray diffraction efficiency is highly sensitive to the parameters of the two-temperature model. As an example, a lower electron–phonon coupling factor allows the electrons to diffuse further into the sample before their energy is transferred to the lattice, which gives rise to heat deposition profile extending deeper into the sample. In the simulations, we set the electron–phonon coupling factor G as the free parameter, the laser fluence was set as a free parameter within the experimental uncertainty and all other parameters are given in Table I. The best fit to the experimental data was obtained for $G = 9 \times 10^{16}$ W/m^3 K with an uncertainty of $\pm 2 \times 10^{16}$ W/m^3 K. When values of G are within the error bar, the simulated and experimental X-ray diffraction efficiencies are in agreement, but when values of G lie outside the error bar, the simulation results start to deviate significantly from the experiment. The value of G is lower than those measured previously by Beaurepaire *et al*.,[21] Wellershoff *et al*.,[22] Saito *et al*.,[23] Caffrey *et al*.,[15] and Hopkins *et al*.[24] (see Table II). In Table II it can be seen that a wide range of film thickness and fluencies have been used for the previous studies. In the studies cited, different methods and observables have been used. Beaurepaire *et al*.[21] detected electron and spin temperatures, Caffrey *et al*.[15] and Hopkins *et al*.[24] detected electron and lattice temperatures whereas the study by Wellershoff *et al*.[22] is based on damage thresholds. The conditions in the measurement by Saito *et al*.[23] mostly resemble ours in terms

TABLE II. Previously measured values of the electron–phonon coupling factor, G, in nickel.

Source	Beaurepaire *et al.*[21]	Wellershof *et al.*[22]	Saito *et al.*[23]	Caffrey *et al.*[15]	Hopkins *et al.*[24]
G [W/m^3 K]	80×10^{16}[a]	36×10^{16} $\pm 14 \times 10^{16}$ (40%)	44×10^{16}[b]	105×10^{16} $\pm 5 \times 10^{16}$	35.5×10^{16} $\pm 3.6 \times 10^{16}$ (10%)
Fluence [mJ/cm^2]	7	8–22	0.01	0.1372	0.5
Wavelength [nm]	620	400	415	750–782	800
Ni thickness [nm]	22	10–200[c]	200	22	30–50[d]
Measurement technique	Optic and magneto-optical pump-probe techniques	Optical damage thresholds	Interferometric probing	Transient thermo-reflectance	Transient thermo-reflectance
Measurement sensitive to	T_e, T_{spin}	T_l	Acoustic strain pulse	T_e, T_l	T_e, T_l
A_e [J/m^3 K^2]	6000	…	1065	1065	…
Time measurement window [ps]	0–8	Non-time dependent measurement	0–200	0–4	0–5

[a]Also determined electron-spin coupling factor 60×10^{16} W/m^3 K and spin-phonon coupling factor 2×10^{16} W/m^3 K.
[b]Theoretical value used when reproducing their data with simulation.
[c]Film thicknesses: 10 nm, 20 nm, 30 nm, 40 nm, 50 nm, 60 nm, 70 nm, 80 nm, 90 nm, 100 nm, 200 nm.
[d]Film thicknesses: 30 nm, 40 nm, 50 nm.

of film thickness and method, since they also observed an acoustic response in the lattice. However, the fluence was about three orders of magnitude lower in their study. The high fluence used in our study gives a higher electron temperature compared to the other studies. Lin *et al.*[25] have found that for Ni, a higher electron temperature leads to a lower electron-phonon coupling factor. As seen in Table II, there is a discrepancy in the values of G at low electron temperatures, but according to Lin *et al.*[25] one could expect a reduction of G by almost a factor three at $T_e = 1500$ K, which is our estimated electron temperature. There has not been an experimental study of G as function of electron temperature, but Hopkins *et al.*[24] saw a tendency of higher electron-phonon coupling factor for lower electron temperatures, but it was within their experimental uncertainty. We believe that our value is applicable for the given excitation conditions and film thickness.

In conclusion, we have demonstrated that the heat deposition in solid films can be investigated by time-resolved X-ray diffraction. This provides a method of determining the electron–phonon coupling factor and electron diffusion dynamics under intense laser excitation, where the initial electron temperature exceeds 1000 K. This was achieved by modelling, using the well-known two-temperature model.

The authors would like to thank the Swedish Research Council (VR), Knut and Alice Wallenberg's Foundation, the Crafoord Foundation, Stiftelsen Olle Engkvist byggmästare and the X-PROBE Marie Skłodowska-Curie ITN within Horizon 2020 for financial support.

[1]O. B. Wright, Phys. Rev. B **49**(14), 9985–9988 (1994).
[2]G. Tas and H. J. Maris, Phys. Rev. B **49**(21), 15046–15054 (1994).
[3]C. Suárez, W. E. Bron, and T. Juhasz, Phys. Rev. Lett. **75**(24), 4536–4539 (1995).
[4]M. Bonn, D. N. Denzler, S. Funk, M. Wolf, S. S. Wellershoff, and J. Hohlfeld, Phys. Rev. B **61**(2), 1101–1105 (2000).
[5]M. Nicoul, U. Shymanovich, A. Tarasevitch, D. von der Linde, and K. Sokolowski-Tinten, Appl. Phys. Lett. **98**(19), 191902 (2011).
[6]R. W. Schoenlein, W. Z. Lin, J. G. Fujimoto, and G. L. Eesley, Phys. Rev. Lett. **58**(16), 1680–1683 (1987).
[7]J. Hohlfeld, S. S. Wellershoff, J. Güdde, U. Conrad, V. Jähnke, and E. Matthias, Chem. Phys. **251**(1–3), 237–258 (2000).
[8]A. M. Lindenberg, I. Kang, S. L. Johnson, T. Missalla, P. A. Heimann, Z. Chang, J. Larsson, P. H. Bucksbaum, H. C. Kapteyn, H. A. Padmore, R. W. Lee, J. S. Wark, and R. W. Falcone, Phys. Rev. Lett. **84**(1), 111–114 (2000).
[9]C. Rose-Petruck, R. Jimenez, T. Guo, A. Cavalleri, C. W. Siders, F. Raksi, J. A. Squier, B. C. Walker, K. R. Wilson, and C. P. J. Barty, Nature **398**(6725), 310–312 (1999).
[10]M. Bargheer, N. Zhavoronkov, Y. Gritsai, J. C. Woo, D. S. Kim, M. Woerner, and T. Elsaesser, Science **306**(5702), 1771–1773 (2004).
[11]J. Larsson, A. Allen, P. H. Bucksbaum, R. W. Falcone, A. Lindenberg, G. Naylor, T. Missalla, D. A. Reis, K. Scheidt, A. Sjogren, P. Sondhauss, M. Wulff, and J. S. Wark, Appl. Phys. A **75**(4), 467–478 (2002).
[12]Y. Gao and M. F. DeCamp, Appl. Phys. Lett. **100**(19), 191903 (2012).
[13]A. I. H. Persson, H. Enquist, A. Jurgilaitis, B. P. Andreasson, and J. Larsson, J. Appl. Phys. **118**(18), 185308 (2015).
[14]S. I. Anisimov, B. L. Kapeliovich, and T. L. Perel'man, Sov. Phys.-JETP **39**(2), 375–377 (1974).
[15]A. P. Caffrey, P. E. Hopkins, J. M. Klopf, and P. M. Norris, Microscale Thermophys. Eng. **9**(4), 365–377 (2005).
[16]C. Thomsen, H. T. Grahn, H. J. Maris, and J. Tauc, Phys. Rev. B **34**(6), 4129–4138 (1986).
[17]M. Harbst, T. N. Hansen, C. Caleman, W. K. Fullagar, P. Jönsson, P. Sondhauss, O. Synnergren, and J. Larsson, Appl. Phys. A **81**(5), 893–900 (2005).
[18]I. M. Lifshits, M. I. Kaganov, and L. V. Tanatarov, Sov. J. At. Energy **6**(4), 261–270 (1960).
[19]S. A. Stepanov, Proc. SPIE **5536**, 16–26 (2004).
[20]D. Schick, A. Bojahr, M. Herzog, R. Shayduk, C. von Korff Schmising, and M. Bargheer, Comput. Phys. Commun. **185**(2), 651–660 (2014).
[21]E. Beaurepaire, J. C. Merle, A. Daunois, and J. Y. Bigot, Phys. Rev. Lett. **76**(22), 4250–4253 (1996).
[22]S. S. Wellershoff, J. Gudde, J. Hohlfeld, J. G. Muller, and E. Matthias, Proc. SPIE **3343**, 378–387 (1998).
[23]T. Saito, O. Matsuda, and O. B. Wright, Phys. Rev. B **67**(20), 205421 (2003).
[24]P. E. Hopkins, J. M. Klopf, and P. M. Norris, Appl. Opt. **46**(11), 2076–2083 (2007).
[25]Z. Lin, L. V. Zhigilei, and V. Celli, Phys. Rev. B **77**(7), 075133 (2008).
[26]C. Kittel, *Introduction to Solid State Physics*, 7th ed. (John Wiley & Sons, Inc., 1996).
[27]W. M. Haynes, in *CRC Handbook of Chemistry and Physics*, edited by W. M. Haynes, 96th ed. (CRC Press/Taylor and Francis, Boca Raton, FL, 2016) (Internet Version 2016).
[28]L. J. Slutsky and C. W. Garland, Phys. Rev. **113**(1), 167–169 (1959).
[29]M. E. Straumanis and C. D. Kim, J. Appl. Phys. **36**(12), 3822–3825 (1965).